Sustainable Energy & Fuels

PAPER

View Article Online
View Journal | View Issue

Cite this: *Sustainable Energy Fuels*, 2017, **1**, 119

Formation, location and beneficial role of PbI_2 in lead halide perovskite solar cells†

Tian Du,[ab] Claire H. Burgess,[a] Jinhyun Kim,[b] Jiaqi Zhang,[a] James R. Durrant[b] and Martyn A. McLachlan*[b]

Received 31st October 2016
Accepted 19th January 2017

DOI: 10.1039/c6se00029k

rsc.li/sustainable-energy

Here we report the investigation of controlled PbI_2 secondary phase formation in $CH_3NH_3PbI_3$ (MAPI) photovoltaics through post-deposition thermal annealing, highlighting the beneficial role of PbI_2 on device performance. Using high-resolution transmission electron microscopy we show the location of PbI_2 within the active layer and propose a nucleation and growth mechanism. We discover that during the annealing that PbI_2 forms mainly in the grain boundary regions of the MAPI films and that at certain temperatures the PbI_2 formed can be highly beneficial to device performance – reducing current–voltage hysteresis and increasing the power conversion efficiency. Our analysis shows that the MAPI grain boundaries as susceptible areas that, under thermal loading, initiate the conversion of MAPI into PbI_2.

Introduction

Lead halide perovskite solar cells have created significant interest since they were first proposed a little more than 5 years ago, such that now they are being referred to the next big thing in the photovoltaics industry.[1] The methylammonium lead halide system has been most commonly reported *i.e.* $CH_3NH_3PbX_3$ (X = I, Br, Cl), although other mixed halide perovskites including $CH_3NH_3PbI_{3-x}Cl_x$,[2] $CH_3NH_3PbI_{3-x}Br_x$,[3] as well as formamidinium tri-iodide perovskite $HC(NH)_2PbI_3$ have also been reported.[4] Current state-of-the-art power conversion efficiencies exceed 20% in these systems,[5,6] a remarkable achievement given that fabrication is enabled through facile solution processing routes, which have remarkable cost saving implications compared with incumbent photovoltaic technologies.[7]

Post-deposition thermal annealing of the perovskite active layers has emerged as a key step in performance enhancement and film stabilization in (i) the numerous solution based processing routes implemented, these include: one-step spin-coating,[8] two-step sequential deposition,[9] and solvent-engineering spin-coating[10] and (ii) the materials systems thus far developed *i.e.* $CH_3NH_3PbI_{3-x}Cl_x$,[8] $CH_3NH_3PbI_3$,[10] and $HC(NH)_2PbI_3$.[4] Unsurprisingly, a variety of annealing regimes have emerged with typical temperatures in the range 70–150 °C,[4,8] and times from 10 minutes to >1 hour,[9,11] in all cases the annealing step is cited as being essential for improving power conversion efficiency (PCE) and reducing current density–voltage (*J*–*V*) hysteresis.[12] Regardless of the annealing conditions cited it is apparent that this processing has a profound impact on film morphology, crystallinity and homogeneity of the perovskite layers resulting in a dramatic impact on measured device performance.[13] In parallel, it has been observed that excessive or secondary annealing can decompose the active layer, irreversibly forming species including PbI_2. This is exemplified by post-annealing at elevated temperature, 150 °C, for a few minutes[14] or lower temperatures, ~100 °C, for extended periods[15] where the formation of a secondary PbI_2 phase is observed. To compound this issue thermally induced decomposition can be accelerated by the presence of illumination,[16] moisture,[17] and interfacial alkaline ligands,[18] and is known to occur even at 85 °C, the upper limit of standard thermal cycling tests in inert atmosphere.[19] These observations are made despite the reported decomposition temperature of $CH_3NH_3PbI_3$ being close to 300 °C, clearly degradation occurs below 100 °C,[20] perhaps at sites such as grain boundaries,[21] surfaces and interfaces. The generation of PbI_2 secondary phase should therefore be considered not only in post-deposition treatments but also during the operation under environmental and/or thermal stress.

Degradation of the perovskite absorber may therefore seem like something to be avoided, however the presence of PbI_2 can actually be beneficial to device performance. For example Chen *et al.* have shown impressive PCE improvements, 0.66% to 12%, by thermally forming PbI_2, which is attributed to surface defect passivation.[22] Alternatively, PbI_2 can also be incorporated into perovskite absorbers by adding excess PbI_2 to the precursor solution, which has been proposed as a means of reducing *J*–*V* hysteresis by blocking ionic migration.[23] As a further example, unreacted PbI_2 remaining as a secondary phase during dip-coating, is reported to suppress charge carrier recombination at

[a]*Department of Materials and Centre for Plastic Electronics, Imperial College London, SW7 2BP, UK*

[b]*Department of Chemistry and Centre for Plastic Electronics, Imperial College London, SW7 2AZ, UK. E-mail: martyn.mclachlan@imperial.ac.uk*

† Electronic supplementary information (ESI) available. See DOI: 10.1039/c6se00029k

the perovskite/cathode interface thus enhancing device performance.[24]

Herein, we report the investigation of controlled PbI_2 secondary phase formation in $CH_3NH_3PbI_3$ (MAPI) photovoltaics through post-deposition annealing, highlighting the beneficial role of PbI_2 and through the use of high resolution transmission electron microscopy propose a nucleation and growth mechanism for PbI_2. In summary the MAPI films were prepared *via* a "toluene-dripping" method reported by Jeon *et al.*[10] following which brief (20 s) anneal at 100 °C was carried out on which the color of films changed from pale yellow to a characteristic dark brown. We have investigated the influence of a subsequent thermal anneal between 100–150 °C for 10 minutes. We discover that during the second annealing step PbI_2 forms mainly in the grain boundary regions of the MAPI films and that at certain temperatures the PbI_2 formed can be highly beneficial to device performance. Our analysis shows that the MAPI grain boundaries as susceptible areas that, under thermal loading, initiate the conversion of MAPI into PbI_2.

Results and discussion

Typical X-ray diffraction patterns of the post-annealed MAPI films are shown in Fig. 1a. The films annealed at 100 °C and 110 °C show the presence of polycrystalline MAPI with the (110) diffraction peak clearly visible around 14.2° (2θ). As temperature is increased a (001) diffraction peak of PbI_2 appears around 12.5° (2θ), which increases with intensity as temperature is raised, at 150 °C the (101) and (003) peaks of PbI_2 are also visible. Based on these data we suggest that post-deposition annealing leads to the thermal decomposition of MAPI to CH_3NH_3I (MAI) and PbI_2. The MAI is vaporized from the film due to its low sublimation temperature whilst the inorganic PbI_2 remains in the film resulting films, as confirmed by the powder diffraction patterns of PbI_2 and CH_3NH_3I (MAI) in ESI Fig. S1.† Interestingly the tetragonal structure of the MAPI is preserved on annealing, evidenced by the clear separation of the (211) and (112) diffraction peaks which may indicate that the nature of MAPI in the bulk of the films remains unchanged. We observe that PbI_2 formation appears to be a kinetically dominated process, where the content of PbI_2 secondary phase in MAPI films can be increased by either elevating the temperature or prolonging the time of post annealing.[22]

Fig. 1b shows surface scanning electron microscopy (SEM) images of MAPI films deposited on a compact TiO_2 layer annealed between 100–150 °C. The pristine film (100 °C) shows a relatively flat surface with large, well-defined MAPI grains visible. As the temperature of post-annealing increases the surface homogeneity changes with an enlargement in grain size coupled with the presence of smaller granular features and pinholes. In combination with the XRD data we propose that the smaller grains and surface features (Fig. 1b) may be PbI_2. Similarly, previous studies have highlighted the presence of comparable surface features[22,25] However, the presence of PbI_2 cannot be unambiguously confirmed using the SEM, either in imaging or analytical modes owing to the contribution from the surrounding MAPI contributing to signal that could be detected using *e.g.* energy dispersive X-ray (EDX) analysis.

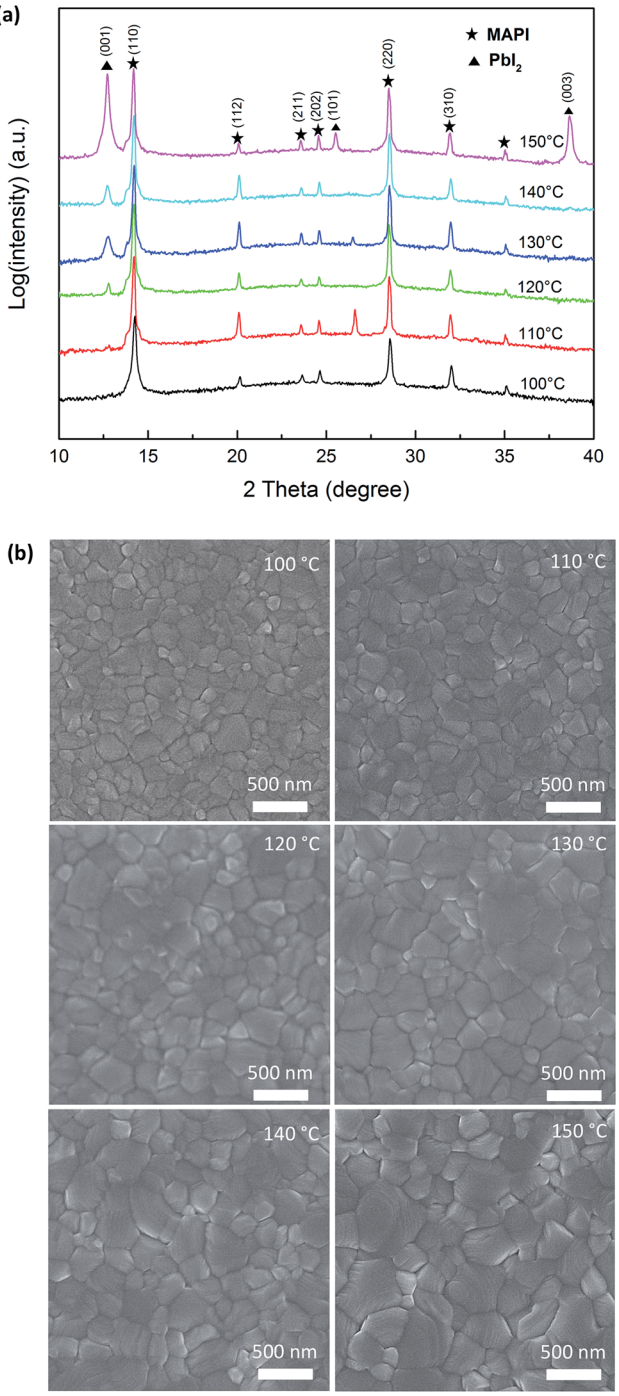

Fig. 1 (a) X-ray diffraction patterns of the post-annealed $CH_3NH_3PbI_3$ (MAPI) lead halide perovskite films deposited on a compact TiO_2 layer. (b) Top-view scanning electron microscopy (SEM) images of MAPI films on TiO_2 compact layer after post-annealing over the temperature range 100–150 °C.

To confirm the identity and location of the secondary phase we implemented scanning transmission electron microscopy (STEM) combined with high resolution transmission electron microscopy (HRTEM) to image the cross-section of glass/c-TiO_2/

$CH_3NH_3PbI_3$/Spiro-OMeTAD structure prepared using focused ion beam (FIB) milling. Fig. 2a and b show the dark-field STEM images of the cross section, where the MAPI layer was post-annealed to 130 °C. The MAPI layer shows well-defined, tightly packed MAPI grains with grain boundaries running perpendicular to the substrate, which is similar to the appearance of MAPI films in other TEM studies.[26,27] However, in our 130 °C post-annealed sample, in addition to the MAPI grains we also see areas of PbI_2 accompanied by voids in the film. In Fig. 2a, grains of PbI_2 (circled in red) can be seen at the edge of a MAPI grain. The PbI_2 secondary phase appears brighter than the MAPI in the dark-field images, due to its higher average atomic number (Z). Fig. 2b shows a PbI_2 crystal (dashed circle) penetrating the MAPI layer. It can be seen that where there are PbI_2 crystals there are also neighboring voids within the film, which appear significantly darker in STEM images due to the reduction in amount of material present in that area. We propose that the voids form in the MAPI grains as a consequence of mass transfer into the grain boundary region that initiates at/near the TiO_2 interface. The areas marked "1–4" were probed using HRTEM with the lattice fringes shown in Fig. 2c–f, respectively. The presence of PbI_2 was confirmed by measuring these fringes that contained (101), (001) and (002) planes, while MAPI showed its (220) and (202) planes. The measured d-spacing in HRTEM images were compared with the d-spacings measured from XRD patterns that are listed in ESI Table S1.†[28] Fig. 2c shows a junction between TiO_2, MAPI and PbI_2, and Fig. 2d shows an area further within the MAPI–PbI_2 layer. The PbI_2 is well aligned with the surface of TiO_2, supporting the hypothesis that PbI_2 growth initiates at the interface of MAPI/TiO_2, and subsequently propagate along the grain boundaries, or other interfaces, towards the Spiro-OMeTAD. In Fig. 2e and f, the PbI_2 in the grain boundary shows clear (001) planes that agree with the most intensely observed XRD peaks with the (202) and (220) planes of MAPI also identified.

Combining the SEM images and STEM/HRTEM images, we suggest that post-annealing leads to the formation of a PbI_2 secondary phase that most likely forms in the grain boundaries of the MAPI films nucleating at/near the TiO_2 layer and extending through the grains until it reaches the MAPI surface, as shown schematically in Fig. 3. It is likely that this growth occurs for two principle reasons. Firstly, the grain boundaries provide a fast channel for the migration of lead and iodine ions. Secondly, they are open channels that allow the escape of MAI species when perovskite decomposes. We propose that the formation of PbI_2 starts from the surface of TiO_2 in the MAPI grain boundary region, and gradually propagates through the MAPI accompanied by the formation of a neighboring void. This may be associated with the nature of the chemical environment at this interface or conceivably owing to the thermal gradient that exists as the samples are post-annealed. The small grains observed by SEM in Fig. 1b should indeed be PbI_2 crystals that have grown through the layer, and the pinholes appear when the voids neighboring the PbI_2 reach the film surface.

The presence of PbI_2 required to be advantageous to device operation can be determined through measurements of the device PCE and also considering the changes in observed reduced J–V hysteresis under forward and reverse bias. Fig. 4a shows the forward and reverse scan J–V curves of three devices in which the perovskite absorbers were annealed at 100 °C, 130 °C and 150 °C. ESI Fig. S2† shows the schematic device structure and corresponding cross-sectional SEM images of these structures. The devices demonstrate moderate J–V hysteresis between scans (marked by the arrows on the curves), which is suggested to be an intrinsic character of planar-structured device with TiO_2 as electron accepting layers. The PCE of the three devices under forward scan (FS, short circuit to open

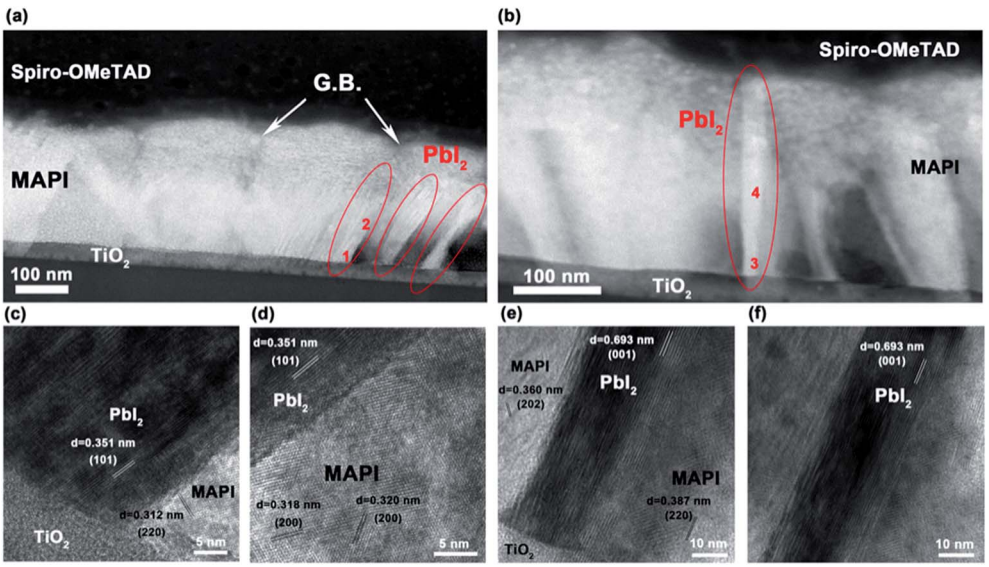

Fig. 2 (a) and (b) Dark-field scanning transmission electron microscopy (STEM) image of the device cross-section, where grain boundaries (G.B) of the MAPI films are marked by arrows and strip-shaped PbI_2 secondary phases are marked by red circles. (c)–(f) High-resolution TEM (HRTEM) images showing the lattice fringes of areas marked 1–4 in (a) and (b), respectively.

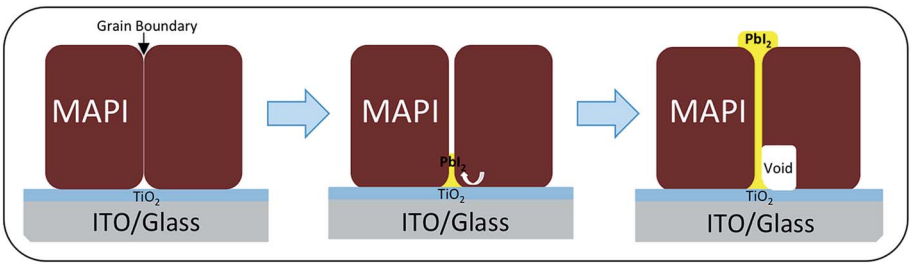

Fig. 3 Schematic illustration of the thermally induced PbI_2 growth process in the grain boundary region of MAPI, we proposer the growth initiates at/near the TiO_2 surface, followed by diffusion of MAPI from the near grain boundary region (arrows) to facilitate the PbI_2 growth eventually propagating to the surface of the MAPI films.

circuit) and reverse scan (RS, open circuit to short circuit) are summarized in the inset table of Fig. 4a. Post-annealing at 130 °C resulted in an improvement in device performance compared with a post-anneal of 100 °C. Further increasing the post-annealing temperature to 150 °C resulted in a drop in device performance. Between 100–130 °C the increased PCE arises from a combination of improved short-circuit current (J_{sc}) and higher fill factor (FF). The considerable improvement of FF was likely due to the PbI_2 secondary phase in grain boundaries blocking shunt pathways.[24] The *J–V* curve of 100 °C post-annealed device is characteristic of a low shunt resistance device. As grain boundaries can be highly conductive, in this state they possibly provide channels that allow direct contact between TiO_2 and Spiro-OMeTAD. The formation of more insulating PbI_2 in the grain boundaries can effectively block the shunt pathways, resulting in remarkable improvement of FF shown in the *J–V* curve of 130 °C post-annealed device. Further heating *i.e.* to 150 °C results in *J–V* curves showing increased series resistance possibly due to the fact that excess PbI_2 increases the electronic resistivity of MAPI films. We note that PbI_2 formation does not sacrifice photocurrent, but rather improves J_{sc}. This is possibly due to enhanced absorption, shown in Fig. 4c, and/or the passivation effect of PbI_2 reported previously.[29] Our *J–V* curves show reduced hysteresis, Fig. 4a, as the post-annealing temperature increased from 100 °C to 150 °C *i.e.* the reduced margin between the *J–V* curves in opposite scan

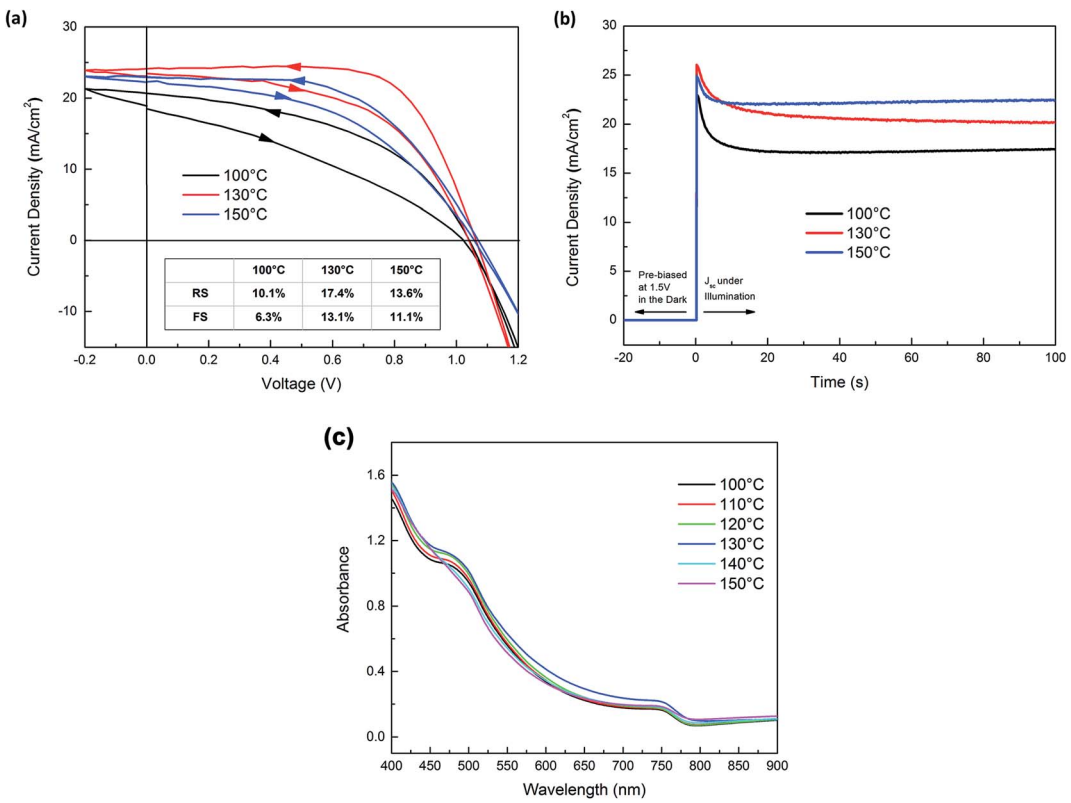

Fig. 4 (a) Cyclic *J–V* scans of lead halide perovskite solar cells with MAPI absorber subjected to post-annealing at 100 °C, 130 °C and 150 °C. (b) Time-resolved photocurrent response of devices with MAPI absorbers post-annealed at 100 °C, 130 °C and 150 °C. (c) Ultraviolet-visible absorbance spectra of MAPI films deposited on compact TiO_2.

direction. The degree of *J–V* hysteresis was more explicitly illustrated by the time-resolved photocurrent response in Fig. 4b. The devices were held at 1.5 V *i.e.* $>V_{oc}$ in the dark and switched to short-circuit condition whilst simultaneously illuminated. The photocurrent response of all devices presented a spike followed by a decay process before reaching steady-state, where the overshoot of photocurrent contributes to the *J–V* hysteresis. The devices annealed at 150 °C showed the smallest photocurrent spike; in contrast the 100 °C devices show the largest. As the origin of *J–V* hysteresis in perovskite solar cells is considered to be a consequence of the migration of ionic species,[30] and grain boundaries are the preferred channels for their migration, we attribute the suppressed *J–V* hysteresis to the PbI_2 in grain boundaries acting to block the motion of ionic species. The absorbance spectra the post-annealed c-TiO_2/MAPI films are plotted Fig. 4c. All films exhibit a clear band-edge transition at ~770 nm, the near band-edge absorbance in clearly improved with increasing annealing temperature. This is possibly due to improved film crystallinity induced by the annealing which, with the PbI_2 growth, may contribute to the higher J_{sc} observed at elevated temperature. Additionally, changes in optical absorption have previously been used to highlight MAPI degradation[2,31] hence we propose that in this case the controlled formation of PbI_2 by moderate post-annealing does not lead to significant degradation of MAPI absorber.

We turn now to consideration of the photophysics of the MAPI films as a function of annealing temperature. Fig. 5a–c show transient absorption (TA) spectra in the visible and near infra-red range (450–800 nm) of the MAPI films with and without Spiro-OMeTAD at 1 ps time after excitation at 380 nm (excitation density: 64 μJ cm^{-2}) as a function of film annealing, whilst Fig. 5d shows the transient kinetics at three probe wavelengths for the 150 °C film. Full TA spectra at various delay times are displayed in ESI Fig. S3,† as well as data lower excitation densities. The TA spectra of MAPI films show two distinct peaks of negative optical density change (ΔOD) at ~480 nm (PB1, high energy photo bleaching) and ~755 nm (PB2, low energy photo bleaching/stimulated emission), respectively. The PB2 is assigned to the band edge transition of MAPI perovskite,[32] while the origin of PB1 is under debate and is possibly due to a transition from a deeper valence band level (referred to hereafter as 'VB1') to the conduction band.[33] The broad positive band in the range of 550–650 nm is due to photoinduced transient absorption.[34]

It is apparent from the red spectra in Fig. 5a–c that as the post-annealing temperature is increased, a new bleaching peak appears at ~502 nm. The peak begins to emerge in the 130 °C annealed MAPI film and increases in intensity at 150 °C (highlighted by arrows). This new peak is clearly separated from the PB1 of MAPI at 480 nm. The peak position, close to the onset of PbI_2 absorption[35,36] and the correlation of its appearance with

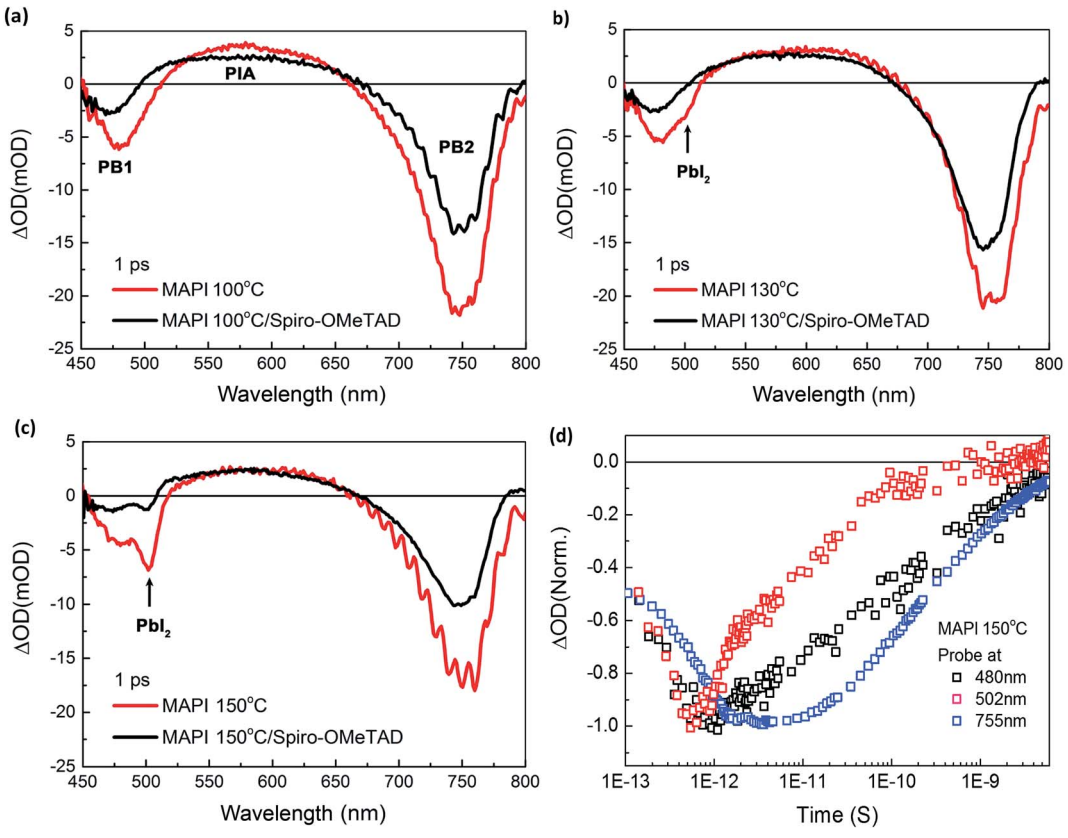

Fig. 5 Transient absorption spectrum at 1 ps (excitation at 380 nm) of MAPI films with and without Spiro-OMeTAD, after annealing at (a) 100 °C, (b) 130 °C, and (c) 150 °C. (d) Transient absorption dynamics of 150 °C-annealed MAPI films probed at 480 nm, 502 nm and 755 nm.

our assays of annealing induced PbI_2 formation detailed above, indicate this 502 nm peak should be assigned to a PbI_2 photobleaching signal. This assignment is in agreement with a previous literature studies, although in this case the peak appearance was not directly correlated with PbI_2 formation.[37] When the same samples were measured with 715 nm rather than 380 nm excitation, the 502 nm peak was no longer observed, whilst the PB1 peak of MAPI at 480 nm remained (ESI Fig. S4†), confirming that the 502 nm peak results from direct excitation of PbI_2, and is distinct from the MAPI secondary bleaching signal PB1. Fig. 5d shows the dynamics of ΔOD decay of the 150 °C post-annealed MAPI film probed at 480 nm, 502 nm and 755 nm. The decay of PbI_2 bleaching (502 nm) was clearly much faster than the decay of the two MAPI bleachings (480 nm and 755 nm), further supporting the different materials origins of these features.

For all samples, the TA spectra of MAPI films with Spiro-OMeTAD show lower ΔOD in both PB1 and PB2 than the spectra of bare MAPI films, Fig. 5a–c, assigned to hole injection into Spiro-OMeTAD from the MAPI. This loss of bleach signal is most pronounced for PB1, particularly as the post-annealing temperature is increased, potentially indicating enhanced hole transfer efficiency from VB1 states. The 502 nm peak signal assigned to PbI_2 photoexcitation was particularly strongly quenched by Spiro-OMeTAD, indicating very efficient hole injection from PbI_2 to Spiro-OMeTAD. It suggests that hole injection from PbI_2 to Spiro-OMeTAD is faster than that from the main valence band of MAPI. The increased quenching of PB1 bleach by Spiro-OMeTAD with increased post-annealing temperature is suggestive that holes from the deeper VB1 may be extracted to extracted to Spiro-OMeTAD *via* PbI_2, in agreement with the dual valence band model proposed by Xing *et al.*[33]

Conclusions

In conclusion, our work shows conclusively that grain boundaries are the preferred locations for PbI_2 nucleation and growth during post deposition thermal anneal of MAPI based perovskite photovoltaic devices. By combining morphological and microstructural analysis, using X-ray diffraction and high-resolution electron microscopy, with transient optical probes we identify the benefits to device performance characteristics enabled by controllably introducing PbI_2 at the grain boundaries. We ascribe our improvements to a combination of beneficial effects, namely (i) PbI_2 increasing the shunt resistance of the active layer, (ii) PbI_2 reducing ionic migration and, (iii) PbI_2 assisting with hole injection into Spiro-OMeTAD. We observe that temperature is an easily accessed parameter for controlling PbI_2 formation and identify an optimum temperature and processing duration. Excessive thermal annealing results in the formation of too much PbI_2 that creates highly resistive devices. Thus by confirming the precise location of PbI_2 in MAPI based perovskite photovoltaics we present a logical explanation of changes in measured performance and optical characteristics and identify optimum processing conditions for producing good devices with low hysteresis.

Experimental

Photovoltaic device fabrication

Indium tin oxide (ITO) substrates (PsioTec, UK) were sequentially cleaned in acetone, isopropanol and deionized water for 10 minutes each using ultrasonics. The substrates were dried by nitrogen gas flow then treated by UV-ozone before film deposition. A compact TiO_2 blocking layer (TiO_2-BL) was prepared by a sol–gel method. Briefly, 350 μl titanium isopropoxide (Aldrich) was mixed with 2.5 ml anhydrous ethanol then 2.5 ml of anhydrous ethanol containing 35 μl hydrochloride acid (HCl) was added. The mixed solution was stirred for 60 minutes and filtered before deposition. The TiO_2-BL film was formed by spin-coating the precursor solution on ITO substrates at 3000 rpm for 30 seconds and subsequently sintering at 500 °C for 30 minutes.

The precursor of organic–inorganic perovskite was prepared by co-dissolving 1.25 M lead iodide (PbI_2, Aldrich) and methylammonium iodide (MAI, Solaronix) in a mixed solvent of gamma-butyrolactone and dimethyl sulfoxide (Aldrich, 7 : 3 by volume). The solution was stirred for 2 hours and was filtered before use. The active layer was formed *via* the "toluene-dripping" method reported by Jeon *et al.*[10] The precursor solution was first spun at 500 rpm for 5 seconds and then 2000 rpm for 20 seconds. 50 ml of toluene was instantly dripped onto the film right at the end of second stage of spinning, and followed by spun at 4000 rpm for 20 seconds. The films were transferred onto a hotplate after spin-coating, and was dried at 100 °C for 20 seconds to crystallize the perovskite. The color of films changed from yellow brown to a characteristic dark brown immediately. Finally the devices were annealed at 100–150 °C on a hotplate for 10 minutes. Both the spin-coating and annealing process were carried out in a nitrogen-filled glovebox.

The hole transport material was prepared by dissolving 82 mg 2,2′,7,7′-tetrakis[*N*,*N*-di(4-methoxyphenyl)amino]-9,9′-spirobifluorene (Spiro-OMeTAD, Borun Chemicals) in 1 ml chlorobenzene. 15.6 μl of bis(trifluoromethane)sulfonimide lithium salt (Li-TFSI, Aldrich) solution (450 mg in 1 ml of acetonitrile) and 24.4 μl of 4-*tert*-butylpyridine (Aldrich) were added to the pristine solution as additives. The solution was stirred for 30 minutes and was filtered before use. The layer was formed by spinning the solution onto the active layer at 3000 rpm for 45 seconds. The devices were stored in dry ambient condition overnight to allow the oxidation of Spiro-OMeTAD. Finally, 60 nm-thick gold was thermally evaporated onto HTM.

Device measurement

Cyclic current density–voltage (*J*–*V*) characteristics were measured by applying external potential bias to the cell and recording the current with a Keithley 2400 source meter. The cells were illuminated by an AM 1.5 xenon lamp solar simulator (Oriel Instruments). The intensity was adjusted to 1 sun by changing the working current, which was calibrated using a Si reference photodiode. All devices were stored in dark prior to measurement and were measured in a nitrogen-filled chamber.

The voltage was scanned from 0 V to 1.5 V, back to −0.2 V and back to 0 V at a scan rate of 125 mV s^{-1}.

Film characterisation

Scanning electron microscopy (SEM) images were obtained using a LEO Gemini 1525 field emission gun scanning electron microscope with a fixed operating voltage of 5 kV. X-ray diffraction (XRD) patterns were obtained using a Bruker D2 diffractometer using a Cu Kα radiation over the 2θ range 10–40°. Cross-sections of the devices were prepared by focused ion beam (FIB) milling using a Helios NanoLab DualBeam instrument. Sequential accelerating voltages of 30, 5 and 2 kV were used for the ion beam. The cross-section was transferred to a JEOL JEM-2100F TEM operated at 200 kV. Low-magnification images were taken under scanning TEM mode, while high-resolution images with lattice fringes were taken under conventional TEM mode. Great care was taken to minimize the exposure of the sample to the electron beam. Ultraviolet-visible (UV-vis) absorbance spectra were obtained by measuring the transmittance of perovskite film from 350–800 nm, with step-size of 1 nm and integrating time of 0.5 s. The films were deposited on glass that was coated by compact TiO_2, and annealed at 100–150 °C, respectively. A diluted precursor solution was used to fabricate MAPI films with three annealing temperatures (100, 130, 150 °C), in order to measure the photo bleaching signal at 450–550 nm. All the samples were kept in the nitrogen-filled glove box in dark for two days after deposition, and were then encapsulated with glass coverslips and Surlyn (Solaronix, Swiss) before measuring in order to prevent the degradation of samples by air. The seal was made by heating the gasket around the cell with the tip of a soldering iron. Femtosecond transient absorption spectra were recorded by using HELIOS (Ultrafast systems). Samples were excited by a pulse train that was generated by an optical parametric amplifier, TOPAS (Light conversion). Both the spectrometer and the optical parametric amplifier were seeded with 800 nm 100 fs pulses at a repetition rate of 1 kHz, generated by a Solstice Ti:Sapphire regenerative amplifier (Newport Ltd). Before and after measuring the fs-TAS, photoluminescence spectroscopy (Horiba Fluorolog system) and electronic absorption spectra (Shimadazu UV-2600) were used to check the optical stability and the material properties.

Acknowledgements

T. D. and M. A. M. are grateful to the Stephen and Ana Hui scholarship (Imperial College) for financial support for PhD studies. C. B. and M. A. M. are grateful to the EPSRC for financial support through the Imperial College DTA scheme/EPSRC Doctoral Prize Fellowship.

References

1 M. A. Green, A. Ho-Baillie and H. J. Snaith, *Nat. Photonics*, 2014, **8**, 506–514.
2 M. M. Lee, J. Teuscher, T. Miyasaka, T. N. Murakami and H. J. Snaith, *Science*, 2012, **338**, 643–647.
3 J. H. Noh, S. H. Im, J. H. Heo, T. N. Mandal and S. Il Seok, *Nano Lett.*, 2013, **13**, 1764–1769.
4 S. Luo and W. A. Daoud, *J. Mater. Chem. A*, 2015, **3**, 8992–9010.
5 N. J. Jeon, J. H. Noh, W. S. Yang, Y. C. Kim, S. Ryu, J. Seo and S. Il Seok, *Nature*, 2015, **517**, 476–480.
6 W. S. Yang, J. H. Noh, N. J. Jeon, Y. C. Kim, S. Ryu, J. Seo and S. I. Seok, *Science*, 2015, **348**, 1234–1237.
7 H. J. Snaith, *J. Phys. Chem. Lett.*, 2013, **4**, 3623–3630.
8 J. M. Ball, M. M. Lee, A. Hey and H. J. Snaith, *Energy Environ. Sci.*, 2013, **6**, 1739–1743.
9 J. Burschka, N. Pellet, S.-J. Moon, R. Humphry-Baker, P. Gao, M. K. Nazeeruddin and M. Gratzel, *Nature*, 2013, **499**, 316–319.
10 N. J. Jeon, J. H. Noh, Y. C. Kim, W. S. Yang, S. Ryu and S. Il Seok, *Nat. Mater.*, 2014, **13**, 897–903.
11 H.-S. Kim, C.-R. Lee, J.-H. Im, K.-B. Lee, T. Moehl, A. Marchioro, S.-J. Moon, R. Humphry-Baker, J.-H. Yum and J. E. Moser, *Sci. Rep.*, 2012, **2**, 591.
12 J. You, Z. Hong, Y. M. Yang, Q. Chen, M. Cai, T.-B. Song, C.-C. Chen, S. Lu, Y. Liu and H. Zhou, *ACS Nano*, 2014, **8**, 1674–1680.
13 A. T. Barrows, A. J. Pearson, C. K. Kwak, A. D. F. Dunbar, A. R. Buckley and D. G. Lidzey, *Energy Environ. Sci.*, 2014, **7**, 2944–2950.
14 G. E. Eperon, V. M. Burlakov, P. Docampo, A. Goriely and H. J. Snaith, *Adv. Funct. Mater.*, 2014, **24**, 151–157.
15 A. Dualeh, N. Tétreault, T. Moehl, P. Gao, M. K. Nazeeruddin and M. Grätzel, *Adv. Funct. Mater.*, 2014, **24**, 3250–3258.
16 C. Bi, Y. Shao, Y. Yuan, Z. Xiao, C. Wang, Y. Gao and J. Huang, *J. Mater. Chem. A*, 2014, **2**, 18508–18514.
17 R. K. Misra, S. Aharon, B. Li, D. Mogilyansky, I. Visoly-Fisher, L. Etgar and E. A. Katz, *J. Phys. Chem. Lett.*, 2015, **6**, 326–330.
18 J. Liu, S. Pathak, T. Stergiopoulos, T. Leijtens, K. Wojciechowski, S. Schumann, N. Kausch-Busies and H. J. Snaith, *J. Phys. Chem. Lett.*, 2015, **6**, 1666–1673.
19 J. Yang, B. D. Siempelkamp, E. Mosconi, F. De Angelis and T. L. Kelly, *Chem. Mater.*, 2015, **27**, 4229–4236.
20 B. Conings, J. Drijkoningen, N. Gauquelin, A. Babayigit, J. D'Haen, L. D'Olieslaeger, A. Ethirajan, J. Verbeeck, J. Manca and E. Mosconi, *Adv. Energy Mater.*, 2015, **5**, 1500477.
21 T. Zhang, N. Guo, G. Li, X. Qian and Y. Zhao, *Nano Energy*, 2016, **26**, 50–56.
22 Q. Chen, H. Zhou, T.-B. Song, S. Luo, Z. Hong, H.-S. Duan, L. Dou, Y. Liu and Y. Yang, *Nano Lett.*, 2014, **14**, 4158–4163.
23 Y. C. Kim, N. J. Jeon, J. H. Noh, W. S. Yang, J. Seo, J. S. Yun, A. Ho-Baillie, S. Huang, M. A. Green and J. Seidel, *Adv. Energy Mater.*, 2015, **6**, 1502104.
24 Y. H. Lee, J. Luo, R. Humphry-Baker, P. Gao, M. Grätzel and M. K. Nazeeruddin, *Adv. Funct. Mater.*, 2015, **25**, 3925–3933.
25 Y. H. Lee, J. Luo, M.-K. Son, P. Gao, K. T. Cho, J. Seo, S. M. Zakeeruddin, M. Grätzel and M. K. Nazeeruddin, *Adv. Mater.*, 2016, **28**, 3966–3972.

26 Y. Zhou, A. L. Vasiliev, W. Wu, M. Yang, S. Pang, K. Zhu and N. P. Padture, *J. Phys. Chem. Lett.*, 2015, **6**, 2292–2297.
27 S. Sun, T. Salim, N. Mathews, M. Duchamp, C. Boothroyd, G. Xing, T. C. Sum and Y. M. Lam, *Energy Environ. Sci.*, 2014, **7**, 399–407.
28 N. Onoda-Yamamuro, O. Yamamuro, T. Matsuo and H. Suga, *J. Phys. Chem. Solids*, 1992, **53**, 277–281.
29 L. Wang, C. McCleese, A. Kovalsky, Y. Zhao and C. Burda, *J. Am. Chem. Soc.*, 2014, **136**, 12205–12208.
30 C. Eames, J. M. Frost, P. R. F. Barnes, B. C. O'regan, A. Walsh and M. S. Islam, *Nat. Commun.*, 2015, **6**, 7497.
31 J. Yang, B. D. Siempelkamp, D. Liu and T. L. Kelly, *ACS Nano*, 2015, **9**, 1955–1963.
32 K. G. Stamplecoskie, J. S. Manser and P. V. Kamat, *Energy Environ. Sci.*, 2015, **8**, 208–215.
33 G. Xing, N. Mathews, S. Sun, S. S. Lim, Y. M. Lam, M. Grätzel, S. Mhaisalkar and T. C. Sum, *Science*, 2013, **342**, 344–347.
34 M. B. Price, J. Butkus, T. C. Jellicoe, A. Sadhanala, A. Briane, J. E. Halpert, K. Broch, J. M. Hodgkiss, R. H. Friend and F. Deschler, *Nat. Commun.*, 2015, **6**, 8420.
35 Y. Zhao, A. M. Nardes and K. Zhu, *Faraday Discuss.*, 2015, **176**, 301–312.
36 T. Liu, Q. Hu, J. Wu, K. Chen, L. Zhao, F. Liu, C. Wang, H. Lu, S. Jia, T. Russell, R. Zhu and Q. Gong, *Adv. Energy Mater.*, 2016, **6**, 1501890.
37 J. A. Christians, P. A. Miranda Herrera and P. V Kamat, *J. Am. Chem. Soc.*, 2015, **137**, 1530–1538.